Helium trapping in carbide precipitates in a tempered F82H ferritic–martensitic steel

B. Mazumder [a], M.E. Bannister [b], F.W. Meyer [b], M.K. Miller [a], C.M. Parish [c], P.D. Edmondson [c,*,1]

[a] Center for Nanophase Materials Science, Oak Ridge National Laboratory, Oak Ridge, TN 37831, USA
[b] Multicharged Ion Research Facility, Oak Ridge National Laboratory, Oak Ridge, TN 37831, USA
[c] Materials Science & Technology Division, Oak Ridge National Laboratory, Oak Ridge, TN 37831, USA

ARTICLE INFO

ABSTRACT

The microstructural changes of a tempered F82H ferritic–martensitic steel following He implantation at 60 and 500 °C have been examined by transmission electron microscopy (TEM) and atom probe tomography (APT). After irradiation at 500 °C, numerous He bubbles were formed throughout the matrix, whereas after irradiation at 60 °C, no bubbles were seen to form in the matrix. In both irradiations, He bubbles were observed to have formed within large carbide precipitates, determined by APT compositional analysis to be $M_{23}C_6$. The observed preferential He bubble formation in carbides during low temperature He irradiation occurs as a result of the diffusing He being trapped in the carbide due to the strong He–C bond. As the He concentration increases in the carbide due to trapping, He bubbles are formed.

Published by Elsevier Ltd. This is an open access article under the CC BY-NC-ND license (http://creativecommons.org/licenses/by-nc-nd/3.0/).

1. Introduction

The materials from which structural components of nuclear reactors will be produced, e.g., reduced activation ferritic–martensitic (RAFM) steels, are subjected to radiation-induced displacement damage as a result of the interactions of energetic neutrons with the material lattice. This displacement damage, which is highly dependent on the irradiation temperature, dose (measured as displacements per atom, or dpa) and dose rates, gives rise to microstructural changes to the lattice in the form of dislocation loops, precipitation formation/dissolution, radiation induced segregation, etc. that can lead to degradation of mechanical properties of the material [1]. Although the structural components of current (Generation III) nuclear power reactors of the BWR and PWR (boiling and pressurised water reactors, respectively) designs typically experience total damage loads of between 10 and 40 dpa at temperatures of 250–350 °C over their operational lifetimes, next generation reactor designs (Generation IV and fusion) are expected to be subjected to up to 200 dpa (and possibly higher) at temperatures of 300–1100 °C [1,2]. This increase in damage level is due to the increased expected lifetimes of the reactor and differences in the neutron energy spectra in *fast* reactor designs, e.g., gas-cooled fast reactor and sodium fast reactor [1].

In addition to the radiation-induced microstructural evolutions given above (n,α), transmutations result in the accumulation of He

that can form pressurised He bubbles that can also degrade the mechanical properties of the host material through swelling, blistering and He embrittlement. This problem is expected to be exacerbated in next generation reactors due to the different neutron spectrum [3,4]. As such, it is imperative that He bubble nucleation and development are understood, so that steps may be taken to mitigate problems associated with He bubble formation, e.g., swelling and He embrittlement, and to manage and mitigate these problems effectively [5–7].

Recently, there has been a substantial research effort examining the viability and effectiveness of nanostructured ferritic alloys (NFAs) to manage He in structural steels [5,7–10]. The application of NFAs for this purpose is predicated on the ultra-fine-dispersion of nano-scale precipitates distributed throughout the matrix acting as effective nucleation sites for nano-scale He bubbles, rather than the random nucleation of larger He bubbles typically observed in traditional steels that do not contain nano-scale precipitates [11–16].

NFAs, such as the 14YWT variant, are effective at trapping and managing the He due to the strong interactions between the vacancies present in the nano-scale Y–Ti–O precipitates that result from the mechanical alloying process [9,17,18]. This has proven to be highly effective at trapping He at the surfaces of the nano-scale precipitates [8]. However, these steels are still in the development phase and rely on expensive processing procedures that are difficult to scale-up to produce foundry-scale components. As a result, it is desirable to investigate novel routes to manage He in other steels that can be produced through traditional casting methods. The work described here concerns a RAFM steel, designated F82H, that has been subjected to He ion irradiation in

---

* Corresponding author.
 E-mail address: edmondsonpd@ornl.gov (P.D. Edmondson).
 [1] At the time of submission, PDE was an Associate Editor of Nuclear Materials and Energy.

Table 1
Elemental composition of the F82H material used in this study. The balance is Fe.

	Cr	C	N	P	S	Al	Si	V	Mn	Ta	W
wt.%	7.44	0.10	0.002	0.001	0.001	0.019	0.14	0.20	0.49	0.04	2.00
at.%	8.02	0.47	0.008	0.002	0.002	0.04	0.28	0.22	0.50	0.012	0.61

Table 2
Table giving the different total fluences ($\times 10^{16}$ ions·cm^{-2}) for each irradiation energy and sample temperature.

Temperature	Ion energy (keV)			
	100	200	300	400
60 °C	1.11	1.05	1.01	1.06
500 °C	1.00	1.10	1.30	1.15

an attempt to elucidate the fundamentals of He bubble gas formation and trapping.

2. Materials & methods

The material used in this study was a F82H steel, with the composition as given by Table 1. Coupons measuring $1 \times 1 \times 0.2$ cm were cut from the parent block and mechanically polished to a mirror-like finish. A final colloidal silica polish was performed to ensure that all mechanical polishing-induced damage was removed from the surface.

Ion irradiations were performed at Oak Ridge National Laboratory's Multicharged Ion Research Facility (MIRF) [19] using an Electron Cyclotron Resonance (ECR) source at multiple energies of 100, 200, 300 and 400 keV He ions to a total average fluence of ~1×10^{16} ions·cm^{-2} (Table 2) to produce an approximately uniform He concentration of 7500–8000 appm and damage of 0.3–0.55 dpa over a depth of between 250 and 900 nm (Fig. 1). The sample temperature during irradiation was maintained at either 60 or 500 °C.
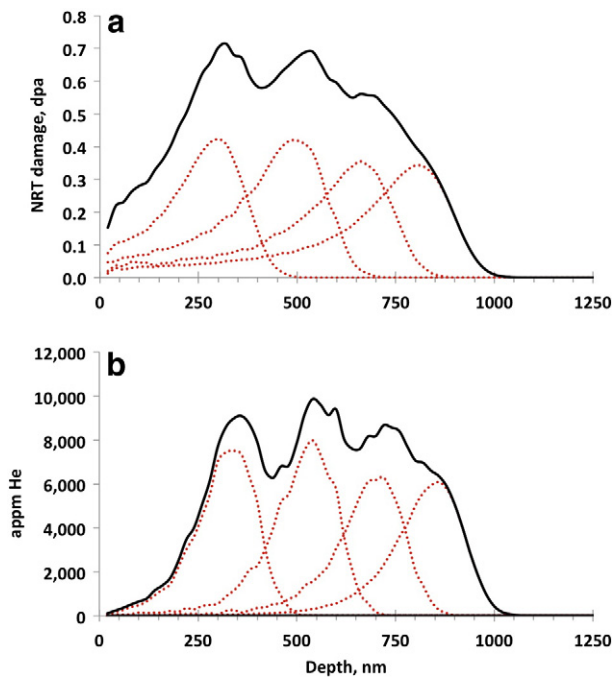

Fig. 2. TEM micrograph of He irradiated F82H. The irradiation was performed at 500 °C. A distribution of He bubbles is observed throughout the matrix and the precipitates, and preferentially at the precipitate/matrix interface. The image is recorded at a depth of 500 nm from the implantation surface.

Information on temperature and fluence measurements, and how the sample is heated can be found elsewhere [19]. Total damage and He concentrations were estimated based on simulations from the Stopping and Ranges of Ions in Matter (SRIM) programme [20]. A displacement energy, E_d, of 40 eV and the simple damage (NRT, or modified Kinchin–Pease) model [21] were used.

The samples to be investigated by atom probe tomography (APT) were prepared by a focused ion beam (FIB) milling technique [22] and analysed in pulsed-laser mode with a Cameca Instruments LEAP™ 4000X HR. The samples were analysed at 30 K, with a laser pulse energy of between 35 and 40 pJ, a pulse frequency of 200 kHz and a detection rate of 0.3–0.5. Density isosurfaces in the range of 40–70 atoms·nm^{-3}

Fig. 3. a) Atom map of the 500 °C He irradiated F82H showing locations of the Fe and Ga atoms. The matrix density isosurfaces indicates the location of He bubbles. b) The low mass portion of the mass spectrum of the analysed volume. A He peak is observed. The He concentration was determined to be 20 appm. Note: Not all He is detected due to loss of He from the bubbles to the vacuum system.

Fig. 1. The dpa damage (a) and the He concentration (b) as a function of depth due to the multiple energy implantations, as predicted by SRIM calculations. Only the Fe and Cr atoms were included in the SRIM calculations. The individual ion energy implantations are shown by the red, dashed lines; the cumulative values shown by the solid black lines.
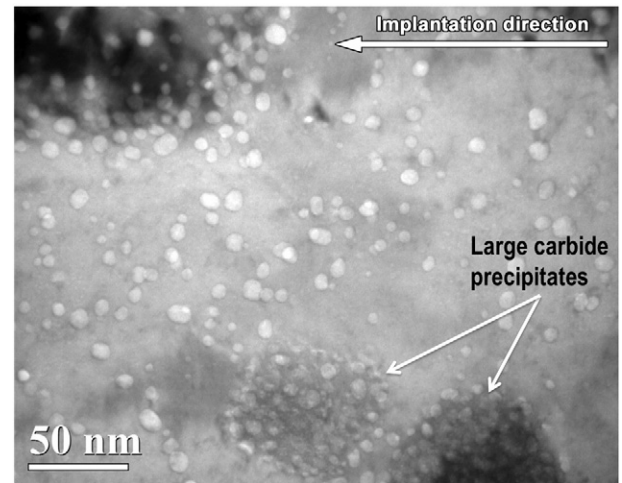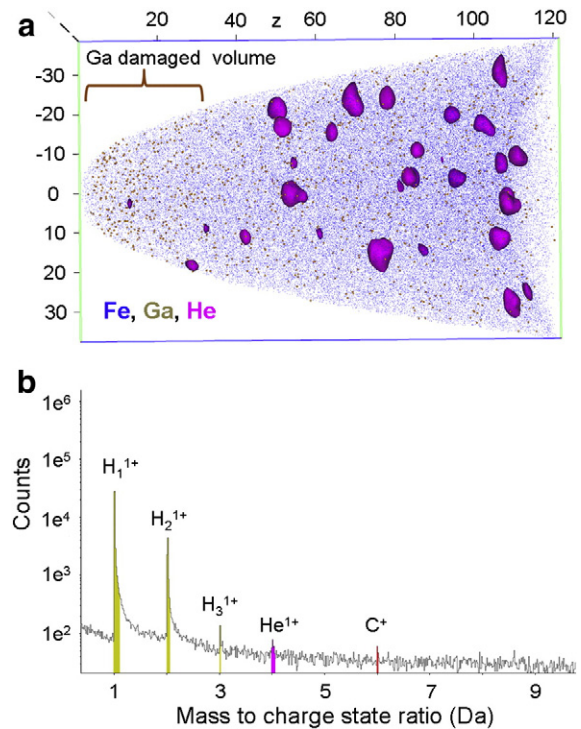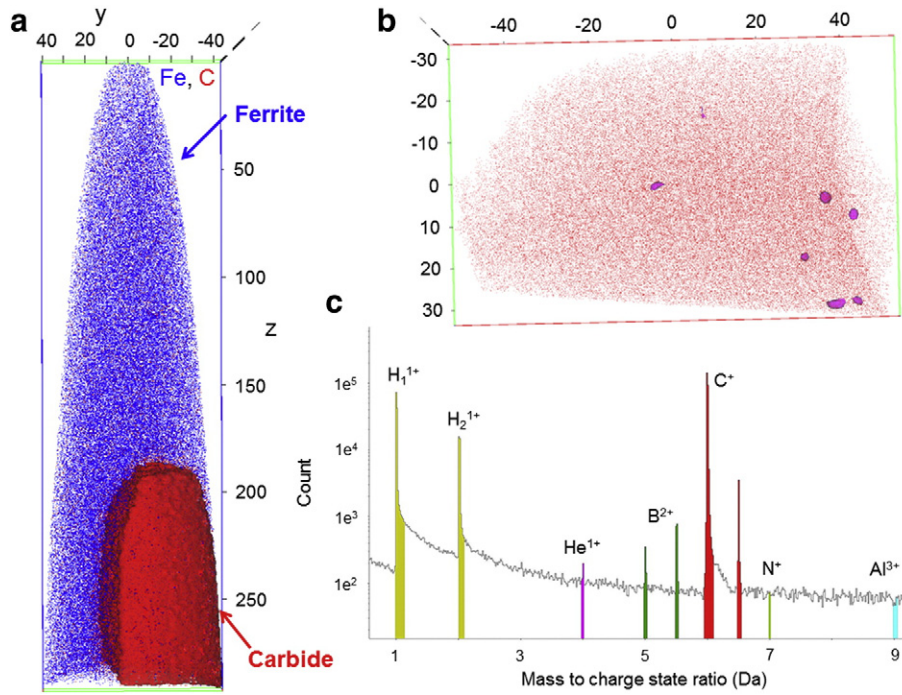
Fig. 4. a) Atom map showing only Fe and C atoms following He irradiation at 60 °C. b) Shows the atom map of C, of the extracted carbide data set, with density isosurfaces identifying regions that represent He bubbles. A value of 50 atoms·nm^{-3} was used to generate these density isosurfaces. c) The low mass portion of the mass spectrum of the carbide indicating the presence of He. The He concentration within the carbide was found to be 40 appm.

were used to identify cavities within the material (interpreted as the presence of He bubbles) [8,23]. The use of density isosurfaces to identify bubbles in materials is necessary because as the specimen material retreats during analysis, the surface of the bubble ruptures causing a loss of the gaseous He from within the bubble. Rather than being ionised and analysed, the He is lost to the vacuum system. The volumes, as determined through the Integrated Visualization & Analysis Software (IVAS), associated with each individual density isosurface are then exported, and the volumes converted to an effective diameter, d_{eff}, using Eq. (1), where V is the volume contained within the density isosurface. The factor '2' in Eq. (1) is used to convert the effective radius into the effective diameter.

$$d_{eff} = 2 \times \sqrt[3]{\frac{3}{4} \frac{V}{\pi}} \qquad (1)$$

Cross-sectional samples to be examined by transmission electron microscopy (TEM) were prepared by FIB milling followed by examination in a Tecnai F20 operating at 200 keV. Images were recorded at a defocus of ± 1 μm to search for, and confirm, the presence of He bubbles through a Fresnel contrast mechanism. The effective He bubble diameters were measured directly from the ImageJ software[2] by taking a line profile scan of the He bubble and measuring the distance between the half maximum intensity peaks, assuming that the He bubbles are perfectly circular in projection (and likewise, spherical).

3. Results & discussion

A TEM micrograph of a specimen irradiated with He at a temperature of 500 °C is shown in Fig. 2. The contrast from the predominantly circular features is characteristic of lower density precipitates, i.e., bubbles or voids, in the matrix. A distribution of relatively large He bubbles can be seen in the matrix. Towards the bottom right of the image – highlighted by two arrows – are two large (50–100 nm diameter) precipitates present

in the material. These precipitates are $M_{23}C_6$-type carbides (see below for more analysis) that have been observed in F82H previously [24]. These precipitates appear to be heavily decorated with He bubbles resulting from the He irradiation, although, due to the two-dimensional nature of TEM micrographs, it is difficult to say definitively. APT data allows for the full three-dimensional reconstruction of the structure of the material analysed, and a representative APT reconstruction of the 500 °C irradiated material is shown in Fig. 3. A number of density isosurfaces representing He bubbles can clearly be seen distributed throughout the matrix. Although large precipitates were observed in the TEM data, no such precipitates were observed in 500 °C APT experiments. This is most likely due to the low number density of these carbides and the small volumes analysed in APT experiments.

An atom probe reconstruction from a dataset obtained from the material irradiated at 60 °C is shown in Fig. 4a: a large carbide can be seen. This carbide was extracted from the volume with the use of a concentration isosurface, as shown from a C atom map in Fig. 4b. Density isosurfaces indicate the presence of cavities within the carbide phase, as shown in Fig. 4b. These cavities are proposed to be He containing
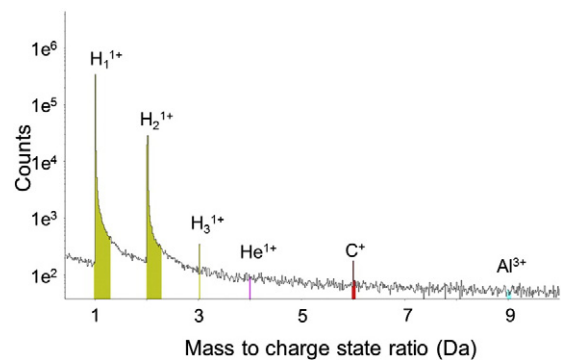

Fig. 5. Low mass portion of the mass spectrum from the matrix shown in Fig. 4. The measured He concentration was 0 appm.

---

[2] Developed by the National Institutes of Health, www.imagej.nih.gov/ij/.
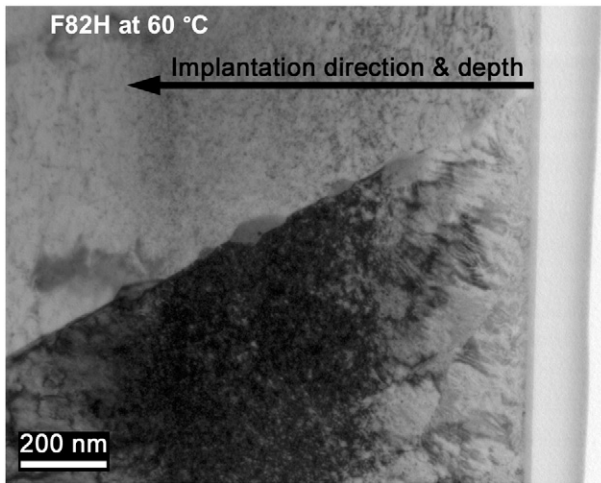
Fig. 6. Under-focus TEM image of the 60 °C He irradiated specimen. No contrast representative of He bubbles is observed. This indicates that resolvable bubbles were not formed i.e., only small He-vacancy clusters were formed.

Table 3
Composition of the carbide observed in Fig. 4 as determined by APT. The balance is made up of trace elements.

Element	at.%	Error
Fe	30.0	0.02
Cr	52.6	0.02
W	4.0	0.01
V	1.0	0.005
Ta	0.0005	0.00
N	0.03	0.003
O	1.9	0.004
C	7.4	0.01

bubbles. He was also detected in the mass spectrum of the carbide (Fig. 4c). It is worth noting that no density isosurfaces were observed in samples that had not been irradiated with He during similar analysis. The low mass portion of the mass spectrum of the matrix is shown in Fig. 5— no He is detected.

He bubbles were observed only within the carbide phase and not in the matrix. TEM analysis of the sample irradiated with He at 60 °C revealed that no He bubbles (within the resolution limit) were formed, as indicated in Fig. 6. Compositional analysis of the carbide present in Fig. 4 is given in Table 3. The C composition of 7.4 at.% is slightly substoichiometric compared to that of a $M_{23}C_6$ carbide precipitate ($[C]$ ~20 at.%). However the Cr concentration is >50% which is commensurate with $M_{23}C_6$ precipitates [25]; and the other solutes in the material (Fe, W, and other minority species) are well known to partially substitute in $M_{23}C_6$ precipitates [26]. Furthermore, the estimated Cr concentration is similar to that obtained from Thermo-calc calculations for a similar composition steel (Fe–9Cr–2W, giving a C concentration in the $M_{23}C_6$ precipitate as 5.21 wt.%) [27]. As such, based on the work presented here and from results in the literature [24], it is highly probable that the precipitates observed in these experiments are of the $M_{23}C_6$-type. Whilst it would be desirable to perform diffraction analyses to confirm these precipitates as $M_{23}C_6$, it was not possible to obtain reliable diffraction data or high resolution transmission electron microscope micrographs on which structural analysis could be performed. However, scanning electron microscopy combined with energy dispersive spectroscopy has previously been used to characterise $M_{23}C_6$ precipitates via chemical means [25] and as such a similar chemical analysis using atom probe data is a viable method of characterising these precipitates as $M_{23}C_6$.

He bubble diameters from both irradiation temperatures, and determined by both TEM and APT, are given in Table 4. The He bubbles formed at the lower temperature irradiation are seen to be significantly smaller than those formed at the higher temperature. The He bubble sizes given compared favourably to those given in the literature for similar irradiation conditions into the same material [13,24,28].

As can be seen from the results presented above, there are clear and distinct differences in the response of the material when irradiated at two different temperatures. At the higher irradiation temperature of 500 °C, nano-scale He bubbles within the range 2–6 nm are formed throughout the matrix whereas at the lower temperature of 60 °C He bubbles are observed to nucleate only within carbide precipitates. Under the implantation conditions used in these experiments, the He concentration and damage are approximately uniform throughout the analysed volume (see Fig. 1), the only variable being the temperatures

at which the specimens were irradiated. It is therefore reasonable to expect that the implanted He is uniformly distributed throughout the matrix. As such it is surprising that it appears that preferential He bubble nucleation in carbides has occurred.

The effect of temperature on He bubble growth is fairly well known [29]. In their work, Iwakiri et al. [29] examined the microstructural evolution of tungsten during low energy (0.25 and 8 keV) He irradiation at temperatures ranging from 25–800 °C. They observed that at ~25 °C, smaller He bubbles were formed compared to those formed during elevated temperature irradiations. This was attributed to tungsten vacancies having no thermal mobility at the low temperature resulting in the bubbles growing through interstitial emission, whereas at the higher irradiation temperatures, He bubble growth resulted from the capture of the thermally mobile, radiation-induced vacancies. Similar effects are also observed when irradiating steels such as HT-9 and EM-12 with He ions [30,31].

It is clear from the results presented in Figs. 4a and 6 that no He bubbles are detected in the matrix or they are below the resolution limits of the techniques used at 60 °C. This does not mean that they are not present, merely that the bubbles are below the minimum threshold size for detection by the techniques being used (i.e., they are in the embryonic state of nucleation). Although it would be desirable to confirm this through analysis using a Friends-of-Friends method [32], no He was seen in the low mass portion of the mass spectrum (Fig. 5), as such this analysis cannot be performed. This is indicative of He not being detected rather than its absence from the sample. As no density isosurfaces with the parameters required to detect cavities/He bubbles were observed during data analysis, this indicates that the He was at a low concentration, i.e., dilute. However, He bubbles are detected in the large carbide visible in the APT reconstruction shown in Fig. 4a–b. This is confirmed by the trace He detected in the mass spectrum of the atoms detected in the carbide regions (Fig. 4c).

This result indicates that there may be three different possibilities for this observation: firstly the possibility of different solubility levels between the matrix and the carbide. Such differences between materials has been observed previously in Cu–Nb multilayers [33] but given that the carbide precipitate in this case is composed of predominantly metal species (~90 at.% metal, see Table 3), it is reasonable to assume that any differences in solubility are negligible.

A second possibility may be the trapping of diffusing He within the carbide precipitate. Here, mobile He that encounters the carbide volume becomes trapped within this volume — it is more energetically favourable to remain contained within the volume rather than re-enter the matrix. This is enhanced by the very strong He–C bond that

Table 4
Average effective diameters of He bubbles, d_{eff}, and their standard deviation as measured in this study. N is the number of bubbles counted to determine these diameters.

	60 °C		500 °C	
	N	d_{eff} (nm)	N	d_{eff} (nm)
TEM	–	–	530	4.73 ± 1.71
APT	7	1.92 ± 0.82	30	4.20 ± 1.46

exists [34]. This would result in an increase in the local concentration of the He within the carbide with bubbles forming as a consequence. This indicates that the preferential formation of He bubbles in carbides results from the strong He–C bond.

Therefore, the observed formation of He bubbles in the carbide during low temperature irradiations is the result of the trapping of diffusing He throughout the matrix. This results in an increase in local He concentration to a level at which He bubbles begin to precipitate.

4. Conclusion

He implantation of an F82H tempered martensitic steel at different temperatures has been conducted, followed by examination using a combination of atom probe tomography and transmission electron microscopy. It was observed that at the lower temperature irradiation (60 °C), detectable bubbles were not observed within the ferrite matrix, but APT revealed the presence of small bubbles within a carbide precipitate. At high temperatures, large bubbles were observed in both the matrix and carbides. It is suggested that preferred bubble nucleation within the carbide precipitate is likely a result of the trapping of He diffusing through the system that then increases in concentration such that He bubbles form. This results in the increase of local He concentration to levels at which He bubbles are formed.

Acknowledgments

References

[1] S.J. Zinkle, G.S. Was, Acta Mater. 61 (2013) 735–758.
[2] S.J. Zinkle, J.T. Busby, Mater. Today 12 (2009) 12–19.
[3] M.R. Gilbert, S.L. Dudarev, S. Zheng, L.W. Packer, J.-C. Sublet, Nucl. Fusion 52 (2012) 083019.
[4] M.R. Gilbert, J.-C. Sublet, Nucl. Fusion 51 (2011) 043005.
[5] G.R. Odette, M.J. Alinger, B.D. Wirth, Annu. Rev. Mater. Res. 38 (2008) 471–503.
[6] G.R. Odette, D.T. Hoelzer, Mater. Nucl. Power 62 (2010) 84–92.
[7] G.R. Odette, P. Miao, D.J. Edwards, T. Yamamoto, R.J. Kurtz, H. Tanigawa, J. Nucl. Mater. 417 (2011) 1001–1004.
[8] P.D. Edmondson, C.M. Parish, Y. Zhang, A. Hallén, M.K. Miller, Scr. Mater. 65 (2011) 731–734.
[9] P.D. Edmondson, C.M. Parish, Y. Zhang, A. Hallén, M.K. Miller, J. Nucl. Mater. 434 (2013) 210–216.
[10] P.D. Edmondson, C.M. Parish, Q. Li, M.K. Miller, J. Nucl. Mater. 445 (2014) 84–90.
[11] T. Yamamoto, G.R. Odette, P. Miao, D.J. Edwards, R.J. Kurtz, J. Nucl. Mater. 386–388 (2009) 338–341.
[12] R.L. Klueh, D.S. Gelles, S. Jitsukawa, A. Kimura, G.R. Odette, B. van der Schaaf, M. Victoria, J. Nucl. Mater. 307–311 (2002) 455–465.
[13] R. Coppola, M. Klimiankou, M. Magnani, A. Möslang, M. Valli, J. Nucl. Mater. 329–333 (2004) 1057–1061.
[14] Y. Katoh, R.E. Stoller, Y. Kohno, A. Kohyama, J. Nucl. Mater. 191–194 (1992) 1144–1149.
[15] Y. Katoh, R.E. Stoller, Y. Kohno, A. Kohyama, J. Nucl. Mater. 210 (1994) 290–302.
[16] N.H. Packan, K. Farrell, J. Nucl. Mater. 85–86 (1979) 677–681.
[17] M.K. Miller, C.L. Fu, D.T. Hoelzer, C.T. Liu, Front. Mater. Sci. Chin. 3 (2009) 9–14.
[18] M.K. Miller, C.L. Fu, X. Chen, Q. Li, Microsc. Microanal. 19 (Suppl. 2) (2013) 1006–1007.
[19] F.W. Meyer, M.E. Bannister, D. Dowling, J.W. Hale, C.C. Havener, J.W. Johnson, R.C. Juras, H.F. Krause, A.J. Mendez, J. Sinclair, A. Tatum, C.R. Vane, E. Bahati Musafiri, M. Fogle, R. Rejoub, H.D. Vergara, L.M. Delaunay, A. Girard, L. Guillemet, J. Chartier, NIMB 242 (2006) 71–74.
[20] J.F. Ziegler, J. Appl. Phys. 85 (1999) 1249–1272.
[21] R.E. Stoller, M.B. Toloczko, G.S. Was, A.G. Certain, S. Dwaraknath, F. Garner, NIMB 310 (2013) 75–80.
[22] M.K. Miller, K.F. Russell, Ultramicroscopy 107 (2007) 761–766.
[23] M.K. Miller, L. Longstreth-Spoor, K.F. Kelton, Ultramicroscopy 111 (2011) 469–472.
[24] X. Jia, Y. Dai, M. Victoria, J. Nucl. Mater. 305 (2002) 1–7.
[25] R.F.A. Jargelius-Pettersson, Z. Metallkd. 79 (1998) 177–183.
[26] T. Sourmail, Mater. Sci. Technol. 17 (2001) 1–14.
[27] S. Ghosh, J. Mater. Sci. 45 (2010) 1823–1829.
[28] T. Yamamoto, Y. Wu, G.R. Odette, S. Yabuuchi, S. Kondo, A. Kimura, J. Nucl. Mater. 449 (2014) 190–199.
[29] H. Iwakiri, K. Yasunaga, K. Morishita, N. Yoshida, J. Nucl. Mater. 283–287 (2000) 1134–1138.
[30] K. Farrell, N.H. Packan, J. Nucl. Mater. 86 (1979) 683–687.
[31] F.A. Smidt Jr., P.R. Malmberg, J.A. Sprague, J.E. Westmoreland, Am. Soc. Test. Mater. (1976) 227.
[32] J.M. Hyde, E.A. Marquis, K.B. Wilford, T.J. Williams, Ultramicroscopy 111 (2011) 440–447.
[33] D. Bhattacharyya, M.J. Demkowicz, Y.-Q. Wang, M. Nastasi, A. Misra, Microsc. Microanal. 18 (2012) 152–161.
[34] C.J. Ortiz, M.J. Caturla, C.C. Fu, F. Willaime, Phys. Rev. B 80 (2009) 134109.